https://doi.org/10.5194/egusphere-2026-5257
Preprint. Discussion started: 14 September 2026

Electrodynamic Reconfiguration of the Polar Ionosphere During the 2021 Antarctic Solar Eclipse

Shibaji Chakraborty[1], Sebastijan Mrak[2], Alex Chartier[2], Evan G. Thomas[3], Gareth Chisham[4], William Bristow[5], and Aroh Barjatya[1]

[1]Embry-Riddle Aeronautical University, Daytona Beach, FL 32114, USA
[2]Applied Physics Laboratory, Johns Hopkins University, Laurel, MD, USA
[3]Dartmouth College, Hanover, NH, USA
[4]British Antarctic Survey, Cambridge CB3 0ET, UK
[5]Department of Meteorology and Atmospheric Science, Pennsylvania State University, PA, USA

Correspondence: Shibaji Chakraborty (chakras4@erau.edu)

Abstract. The 4 December 2021 Antarctic total solar eclipse enhanced anti-sunward polar cap plasma flow, as directly and independently observed by the SuperDARN McMurdo (MCM) radar and the Jang Bogo VIPIR, modulated by eclipse obscuration. AMPERE field-aligned currents (FACs) over the same interval likewise increased with eclipse obscuration, together indicating a possibility of eclipse-driven reconfiguration of polar cap electrodynamics. As supporting, model-dependent context, we combine GITM-derived ionospheric conductance with the AMPERE FACs in a pyMIX potential solver, which shows a loosely corresponding increase in cross-polar-cap potential — consistent with, though not independent confirmation of, the electrodynamic changes observed directly. Separately, the SuperDARN Falkland Islands (FIR) radar observed the sudden emergence of a new 1.5-hop HF propagation mode near the auroral oval boundary during totality and its location of appearance modulated by eclipse obscuration. We examine possible sources of this mode using ray-tracing simulations driven by the same eclipse-modified GITM electron density fields. Together, these multi-instrument observations show that eclipse-driven reduction in ionospheric conductance may drive the coupled magnetosphere–ionosphere (M–I) system through complex, nonlinear adjustment of currents and plasma flow, and that the accompanying changes in ionospheric density can also alter HF propagation conditions.

Keywords. Antarctic Eclipse, Magnetosphere-Ionosphere Coupling, AMPERE Field-Aligned Currents, HF Propagation, Cross-Polar-Cap-Potential, SuperDARN.

1 Introduction

Solar eclipses are semi-periodic geophysical phenomena that offer a unique opportunity to investigate the electrodynamics of the ionosphere. The Moon's shadow temporarily abates incoming solar irradiance, inducing rapid and localized perturbations in the ionosphere–thermosphere (IT) system through alterations in the ionospheric conductivity (e.g., Rishbeth, 1968; Hvoždara and Prigancová, 2002; Chen et al., 2021). These conductivity changes can, in turn, may reconfigure the coupled magnetosphere–ionosphere (M–I) system — altering current systems, cross-polar-cap potential, and possibly the timing of

https://doi.org/10.5194/egusphere-2026-5257
Preprint. Discussion started: 14 September 2026

geomagnetic substorms (Chen et al., 2021; Coyle et al., 2023b, a). This reconfiguration reflects the coupled, mutually regulating relationship between ionospheric conductance and magnetospheric convection (Wolf, 1970; Coroniti and Kennel, 1973), spanning a continuum between idealized voltage-generator (fixed cross-polar-cap potential) and current-generator (fixed field-aligned current) limits, with the cross-polar-cap potential itself known to saturate rather than scale linearly under strong forcing (Lysak, 1985; Siscoe et al., 2002). Eclipse-driven changes also significantly impact high-frequency (HF, 3–30 MHz) radio wave propagation (Moses et al., 2021; Chakraborty et al., 2025) and introduce scintillations in GNSS-derived total electron content (TEC) (e.g., Coyle et al., 2023b; Cnossen et al., 2019); these HF and TEC signatures serve as valuable diagnostics of the underlying conductivity and density perturbations, even though the electrodynamic response of the coupled M–I system is the more fundamental geospace effect.

Polar eclipses are especially compelling in this context, as they modulate geospace electrodynamics along open and high-latitude magnetic field lines, fundamentally different from mid- or low-latitude geometries (Chen et al., 2021; Sun et al., 2021). On these open field lines, the ionosphere connects nearly directly to the solar wind-driven convection electric field, so a local eclipse-driven conductance change is not screened by return currents through a closed magnetosphere the way it would be at lower latitudes, making the polar cap a particularly direct test bed for the voltage-/current-generator continuum described above. Due to their infrequent occurrence, few polar eclipses have been studied in detail, leaving previously under reported phenomena and open questions regarding the full range of magnetospheric responses they can trigger (Coyle et al., 2023a; Sun et al., 2021; Choudhary et al., 2011; Huang et al., 2020). The one existing global simulation study of a polar eclipse's coupled M–I response, for the 10 June 2021 northern polar eclipse, found that eclipse-driven conductance reduction produced large, interhemispherically coupled changes in field-aligned currents, cross-polar-cap potential, and auroral precipitation (Chen et al., 2021); as a model-only study, however, it could not be validated against direct polar-cap observations. Separately, a statistical, population-level analysis found a significant relationship between eclipse timing and geomagnetic substorm onset (Coyle et al., 2023a), though whether an individual substorm occurring near eclipse totality is eclipse-driven, coincidental, or some combination of both remains untested at the level of a single, well-observed event. While eclipse-driven modifications to IT dynamics and their influence on HF communication have been extensively reported, relatively few studies have directly examined how polar eclipses reconfigure the coupled M–I system itself, and none have combined the multi-instrument, ground- and space-based coverage needed to separate an eclipse-driven electrodynamic response from a coincident substorm.

On 4 December 2021, a total solar eclipse passed over the Southern Hemisphere, primarily across the Antarctic continent, offering a rare opportunity to probe eclipse-driven M–I interactions along higher L-shell and open polar field lines. In this study, we combine SuperDARN McMurdo radar and Jang Bogo VIPIR observations with AMPERE field-aligned currents, GITM-derived ionospheric conductance, and a pyMIX potential solver to characterize the eclipse-driven reconfiguration of the polar cap electrodynamic system. We then use SuperDARN Falkland Islands radar observations and PHaRLAP ray-tracing simulations, driven by the same eclipse-modified electron density, as an independent diagnostic of the changes in the ionospheric refractive index and associated HF propagation conditions that accompany this electrodynamic response. Together, these multi-instrument observations and models characterize the ionospheric and magnetospheric response during and after the eclipse, and underscore the need for fully coupled geospace simulations to unravel the underlying physics.

https://doi.org/10.5194/egusphere-2026-5257
Preprint. Discussion started: 14 September 2026

2 Data and Methods

We use observations from the SuperDARN Falkland Islands (FIR) and McMurdo (MCM) HF radars (Greenwald et al., 1985; Chisham et al., 2007; Nishitani et al., 2019) to characterize eclipse-driven changes in HF backscatter and line-of-sight Doppler velocity across the auroral oval and polar cap. Horizontal plasma drift is independently measured by the Jang Bogo VIPIR (Kim et al., 2023), providing a ground-based cross-check on the SuperDARN MCM flow observations. Field-aligned currents (FACs) are obtained from the Active Magnetosphere and Planetary Electrodynamics Response Experiment (AMPERE) (Anderson et al., 2000), giving a direct, model-independent measure of the eclipse-driven current response. We have also used MMS1 ion bulk-flow moments from the Fast Plasma Investigation (FPI) (Pollock et al., 2016) and $E \times B$ drift velocity from the Electric Field Double Probe (EDP) (Lindqvist et al., 2016; Ergun et al., 2016) combined with the fluxgate magnetometer (FGM), together with the GOES-17 geosynchronous magnetometer (H-component) (Singer et al., 1996), as independent context for evaluating whether the observed electrodynamic changes coincide with substorm activity. Figure S1 in the Supplement provides a schematic overview of the event geometry, showing the relative locations of the MCM radar, MMS, and GOES-17 with respect to the modeled dayside and duskside magnetic field lines, the eclipse obscuration centered over the South Pole, and the dawn-to-dusk polar cap convective flow and electric field discussed throughout this study.

We use the Global Ionosphere Thermosphere Model (GITM), implementing the pyEclipse 19.3 nm eclipse occultation mask (Mrak et al., 2018, 2022; Cantrall et al., 2024) at 1.25° lat × 2.5° lon × ¼ scale-height resolution with 1-minute cadence, following the same configuration used for the 2017 eclipse (Mrak et al., 2022). GITM is externally forced by the empirical Weimer (Weimer, 2005) convection potential and the ASHLEY (Zhu et al., 2021) precipitation model, and does not solve M–I coupling self-consistently. We therefore use GITM only to obtain the eclipse-driven Hall and Pedersen conductance and electron density fields; GITM's own (Weimer-forced) potential is not used to infer the eclipse-driven electric field.

Our primary evidence for the eclipse-driven electrodynamic response comes from the SuperDARN MCM radar and Jang Bogo VIPIR plasma-flow observations described above, which directly and independently show enhanced polar cap convection modulated by eclipse obscuration. As supporting context, we also combine GITM-derived conductance with AMPERE FACs as inputs to the pyMIX potential solver (Chartier et al., 2022), which solves for an electrostatic potential, Φ[pyMIX]. Because AMPERE FACs are themselves an input to this solve, Φ[pyMIX] and the FAC intensity are not independent quantities; we treat this pairing loosely, as a qualitative, model-dependent illustration of the current–potential response rather than a primary result. Separately, the GITM electron density field is used as input to 2-D PHaRLAP ray-tracing simulations (Cervera and Harris, 2014) along FIR beam 7 at 12.2 MHz, to interpret eclipse-driven changes in HF propagation; GITM is well suited to this role since ray tracing depends only on the density structure, not on the self-consistency of its internal potential.

3 Observations

Figure 1 shows FoV scan plots from the SuperDARN McMurdo (MCM, blue) and Falkland Islands (FIR, red) radars during the eclipse, overlaid with eclipse obscuration, modeled auroral oval boundaries (Newell et al., 1996, 2009), and horizontal plasma velocity vectors from the Jang Bogo VIPIR (Kim et al., 2023). The MCM radar, oriented sunward within the polar cap,

https://doi.org/10.5194/egusphere-2026-5257
Preprint. Discussion started: 14 September 2026

observed high-velocity ionospheric scatter (IS) directed toward the radar throughout the event, consistent with anti-sunward polar cap plasma flow. Prior to eclipse onset, Doppler velocities were around ∼200 m/s; as the eclipse advanced into the FoV, both the spatial coverage of backscatter and the line-of-sight (LoS) Doppler velocities increased sharply, exceeding 600 m/s and saturating the color scale. The Jang Bogo quiver vectors independently corroborate this enhancement, showing anti-sunward drift modulated by eclipse obscuration. Panels (A–F) span 06:00 to 08:15 UT, capturing the full progression from pre-eclipse background conditions through the peak of totality (∼07:44 UT) and into the early recovery phase. Throughout this progression, the high-velocity MCM echoes remained poleward of the modeled equatorward auroral oval boundary, consistent with polar cap, rather than auroral-zone, convection. These high-velocity echoes remained confined within the polar cap boundary and persisted for several hours before decreasing as the eclipse footprint departed the FoV. Together, MCM and Jang Bogo provide our primary, independent evidence for eclipse-driven enhancement of polar cap convection.

Figure 2 shows the corresponding spatiotemporal evolution of AMPERE FACs and, as supporting context, Φ[pyMIX] over the Antarctic sector (see Data and Methods section for the modeling chain and its caveats). Both FAC intensity and Φ[pyMIX] are loosely modulated by eclipse obscuration: as obscuration increases, FAC intensity and cross-polar-cap potential (CPCP) both increase, and both decrease during the recovery phase. CPCP (ϕ_0) ranges from approximately 38 to 49 kV between 07:00 and 08:00 UT, decreasing to 15.7 kV by 09:00 UT as the eclipse obscuration recedes. Over the same interval, the IMF magnitude and clock angle noted in each panel remain comparatively steady ($|B| \approx$ 3.9–4.4 nT, $\theta \approx$ –26° to –30°), so the panel-to-panel changes in FAC intensity and Φ[pyMIX] most likely track the eclipse obscuration curve rather than any noted change in upstream IMF conditions. We treat this FAC/Φ[pyMIX] pairing as qualitative, model-dependent context for the convection enhancement described above, not as an independent confirmation of it.

Figure 3 presents the same primary quantities shown in Figures 1 and 2, but as continuous time series rather than discrete snapshots, allowing their temporal evolution to be compared directly against eclipse obscuration. Panel (A) shows the range-time evolution of LoS Doppler velocity along MCM beam 7, with vertical dashed black lines marking the start and end of the global eclipse, indicating the total temporal span of the eclipse. Panel (B) shows the horizontal Doppler velocity (v_H) from the Jang Bogo VIPIR alongside a 9-day background average, together with the eclipse obscuration curve over the Jang Bogo station in red. Panel (C) shows AMPERE FAC intensity and Φ[pyMIX] CPCP over the same interval. Across all three panels, MCM velocity, Jang Bogo v_H, FAC intensity, and CPCP each rise and fall in tandem with the obscuration curve directly, increasing through the partial and total eclipse phases and decreasing during the recovery phase, consistent with the snapshot views in Figures 1 and 2. We return to the implications of this joint temporal behavior for M–I coupling in the Discussion section.

Returning to Figure 1, FIR observed predominantly ground scatter (GS) at low Doppler velocities ($|v| \leq$30 m/s), exhibiting a characteristic swing from about –15 m/s to +30 m/s as the eclipse shadow crossed the FoV — consistent with previous eclipse studies (Thomas et al., 2024) and modulated by the rate of change of eclipse obscuration. Unlike earlier eclipse studies, we do not observe a significant shift in GS skip distance, a propagation-geometry factor known to influence high-latitude HF echo characteristics (Ponomarenko et al., 2007). More notably, a new population of high-velocity ionospheric scatter emerged at far ranges near the auroral oval, coincident with eclipse totality and modulated by the obscuration peak (green boxes, Figure 1C–

https://doi.org/10.5194/egusphere-2026-5257
Preprint. Discussion started: 14 September 2026

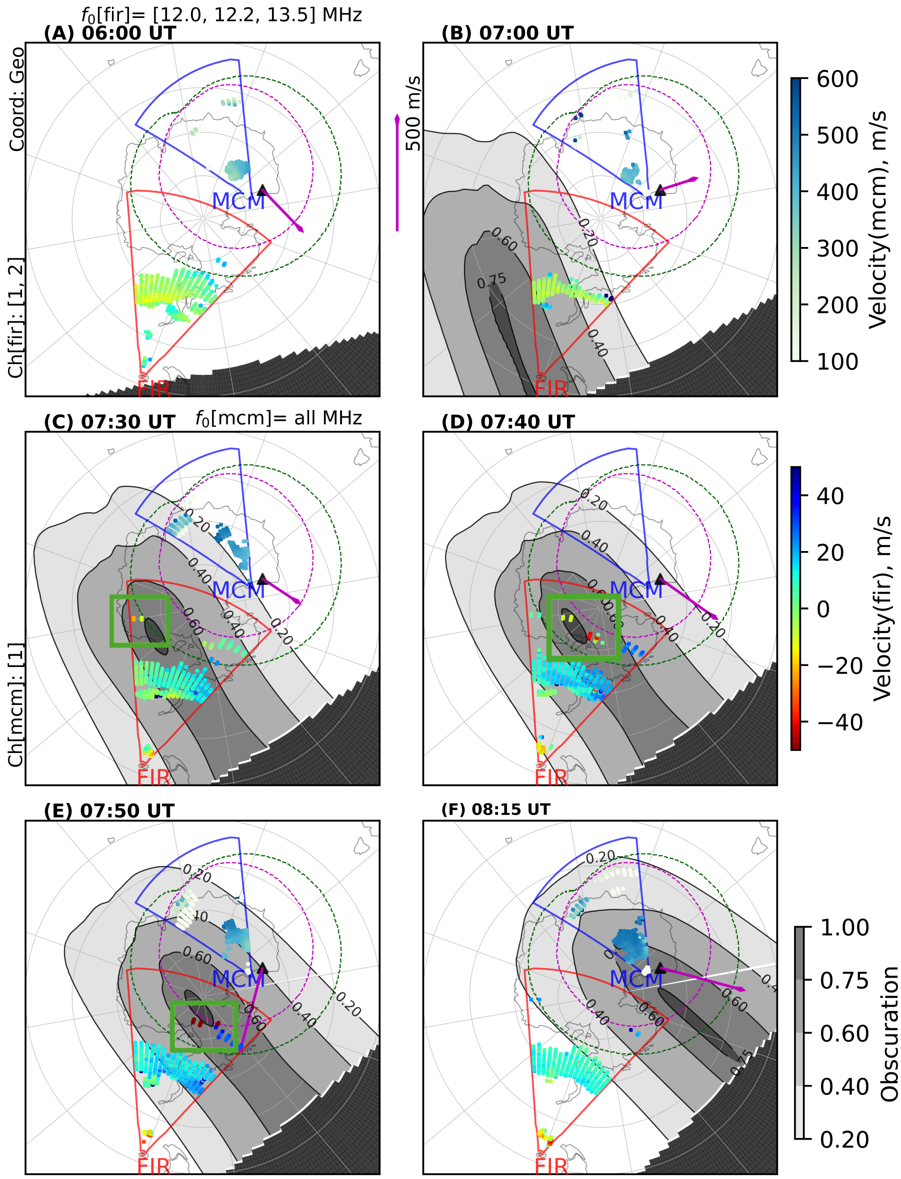

Figure 1. FoV scan plots from the SuperDARN Falkland Island (FIR, in red) and McMurdo (MCM, in blue) radars during the solar eclipse on 04 December 2021. Panels (A–F) present a series of FoV scan plots depicting line-of-sight (LoS) Doppler velocity from the FIR and MCM radars, color-coded according to the scales located right of panel (B) and (D), respectively. The eclipse obscuration is color-coded gray by the color bar in the bottom-right corner. The black shaded region indicates the nightside. Modeled auroral oval boundaries (poleward: magenta, equatorward: green) are shown in each panel. Light green boxes in panels (C–E) indicate high-velocity ionospheric scatter (IS) appearing near the peak of eclipse (EUV) totality. Magenta quiver vectors indicate horizontal plasma velocity observed from the Jang Bogo VIPIR station, overlaid on each panel.

https://doi.org/10.5194/egusphere-2026-5257
Preprint. Discussion started: 14 September 2026

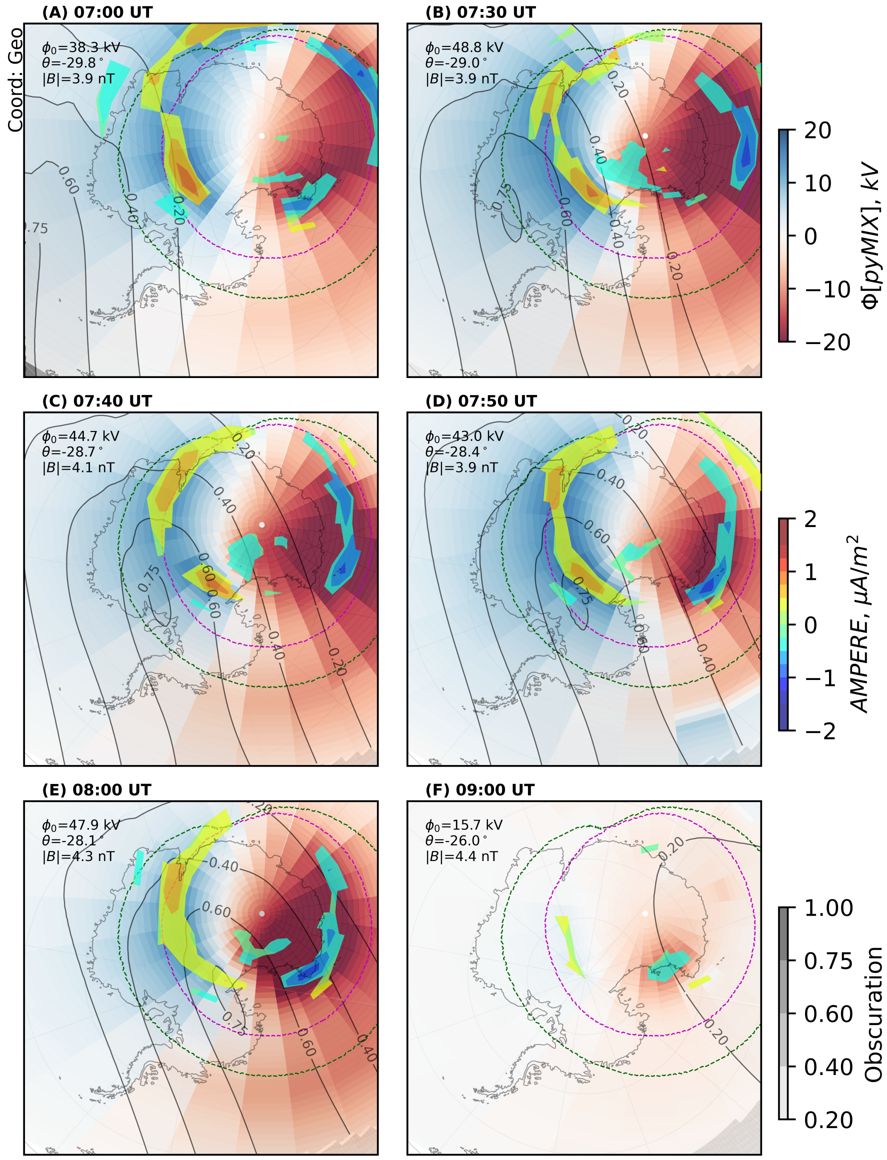

Figure 2. Spatiotemporal variation of fitted potential (in kV) from AMPERE field-aligned currents (FACs) and modeled conductance during the solar eclipse on 04 December 2021 (see Data and Methods section for the pyMIX modeling chain). Panels (A–F) present a series of temporal snapshots showing polar-cap potential (ϕ, in kV) and AMPERE FAC, color-coded according to the scales located right of panel (B) and (D), respectively. The eclipse obscuration is color-coded gray by the color bar in the bottom-right corner. The black shaded region indicates the nightside. CPCP (ϕ_0, in kV), IMF clock angle (θ, in degrees), and IMF magnitude ($|B|$, in nT) are noted in each panel. Magenta and green dashed curves in each panel indicate the poleward and equatorward boundaries of the auroral oval.

https://doi.org/10.5194/egusphere-2026-5257
Preprint. Discussion started: 14 September 2026

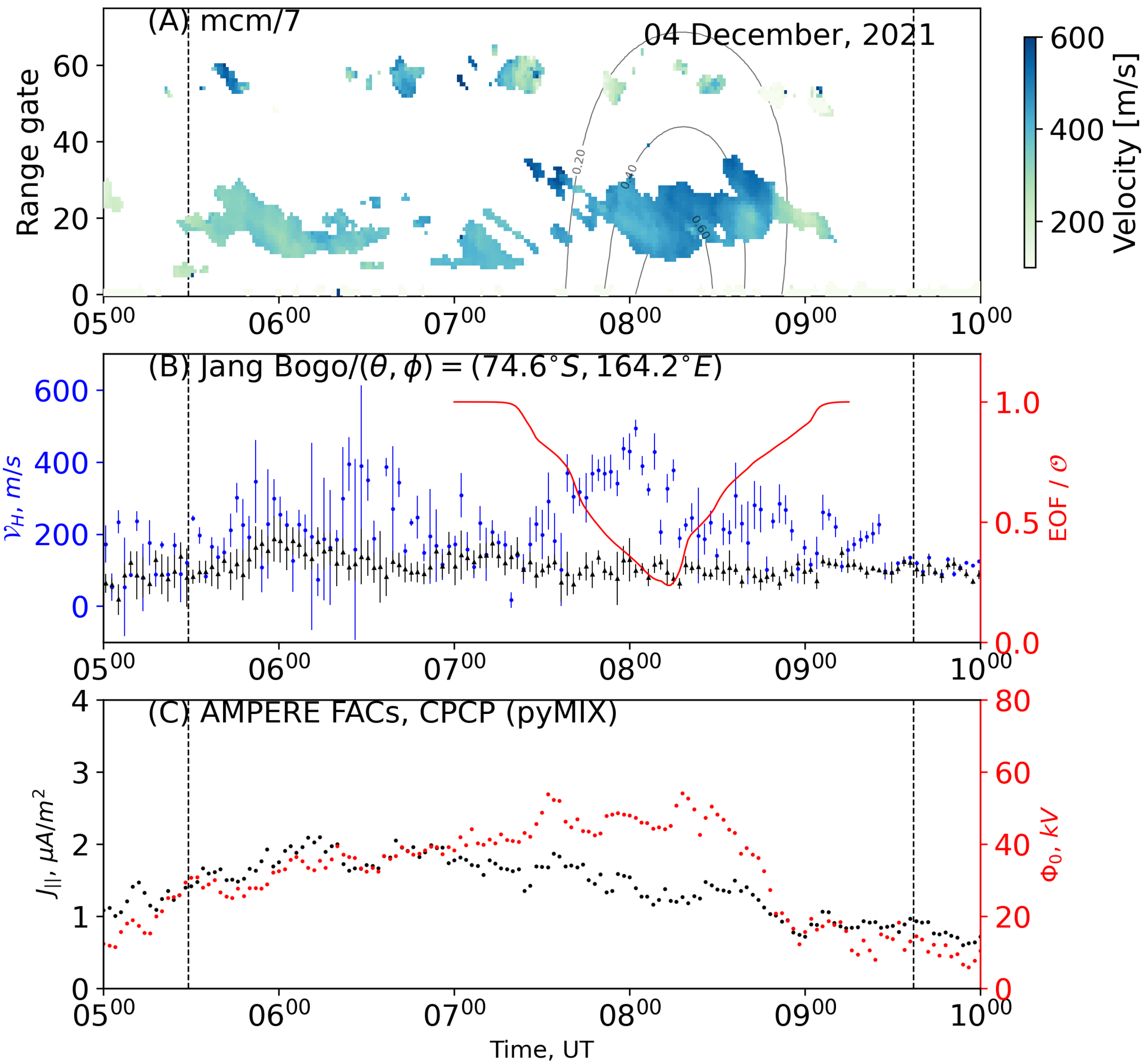

Figure 3. RTI and time series of CPCP and FACs during 4 December 2021. (a) Plasma flow velocity along beam 7 of the MCM radar, color-coded by the color bar on the right, with eclipse obscuration contours overlaid. (b) Horizontal component of Doppler velocity ($v_H = \sqrt{v_x^2 + v_y^2}$) from the Jang Bogo VIPIR (blue), compared against a 9-day background average (black); the red curve indicates eclipse obscuration over the Jang Bogo station. (c) AMPERE field-aligned currents (black) and Φ[pyMIX] cross-polar-cap potential (red). Vertical dashed and solid black lines indicate the start and end of the global partial and total eclipse, respectively; the red vertical line indicates the peak of the eclipse.

https://doi.org/10.5194/egusphere-2026-5257
Preprint. Discussion started: 14 September 2026

E). We examine possible drivers of this feature in Discussion section, including PHaRLAP ray-tracing evidence (Figure 6) for an eclipse-opened 1.5-hop propagation path consistent with the density depletion inferred from the electrodynamic response described above, alongside a possible auroral-precipitation contribution.

Figure 4 examines this high-velocity population across the five FIR operating frequencies available on beam 7. The feature appears as a coherent, strongly negative-Doppler patch (exceeding -50 m/s, locally saturating near -100 m/s) between approximately 07:10 and 08:00 UT at slant ranges of ~3000–3800 km in the 12.0 MHz channel-1 sounding (Figure 4A), the 12.2 MHz channel-2 sounding (Figure 4C), and the 13.5 MHz channel-2 sounding (Figure 4D). The same feature is absent at 10.5 MHz (Figure 4B) and 15.5 MHz (Figure 4E), where only the low-velocity background ground-scatter band is observed over this interval. This frequency-selective appearance, confined to a narrow window between roughly 12 and 13.5 MHz, indicates that the propagation path supporting this scatter opens only over a limited frequency range, consistent with a refractive-index-controlled mechanism rather than a broadband change in radar sensitivity or clutter. We return to this frequency dependence in the Discussion section.

4 Discussion

Solar eclipse mimics a localized day-night transition, which creates a reduction in ionospheric electron content leading up to the peak obscuration, followed by a recovery as the solar disk re-emerges. This study summarizes the eclipse-driven changes in ionospheric propagation conditions and electrodynamics in the south polar regions.

As supporting context for the electrodynamic changes described in Observations section, we next examine whether they coincide with substorm activity using Figure 5, which brings together MMS, GOES-17, AE, and OMNI data across the eclipse interval. Panels (A) and (B) show the location of MMS1 and GOES-17 relative to the Sun–Earth line in GSM X–Y and Y–Z coordinates, confirming MMS was on the dayside/flank rather than in the magnetotail during this interval. Panel (C) shows GOES-17 magnetometer observation (H) together with the AE, AL index and the eclipse obscuration proxy — a light-gray curve tracking the normalized eclipse-obscured area over the dayside ionosphere, used here as a proxy for eclipse progression over the polar ionosphere. Both the AE, AL indices and GOES-17 H profiles track normalized eclipse obscuration proxy closely in shape during this time window. Specifically, GOES-17 H shows a ~15 nT enhancement between approximately 06:40–07:45 UT alongside the AE rise. Panel (D) shows IMF and solar wind conditions, which remain comparatively stable throughout the event window. Panel (E) shows MMS1 ion bulk flow speed and $E \times B$ drift speed; the shaded interval highlights a sudden enhancement in both quantities that coincides with the peak of eclipse obscuration and falls within the active phase of the substorm identified below.

MMS was located near (X, Y, Z) ≈ (0, 14, –12) R_E (GSM) during this interval — outside the magnetotail consistent with its dayside/flank orbit phase for this time of year. The field variability observed there is more consistent with magnetosheath/boundary turbulence tracking upstream solar wind fluctuations than with a magnetotail dipolarization signature. Independent support for this eclipse-driven, rather than substorm-driven, interpretation comes from a concurrent global MHD-GCM simulation of this same event: Hong et al. (2026) likewise found no signature of reconnection onset or dipolarization in

https://doi.org/10.5194/egusphere-2026-5257
Preprint. Discussion started: 14 September 2026

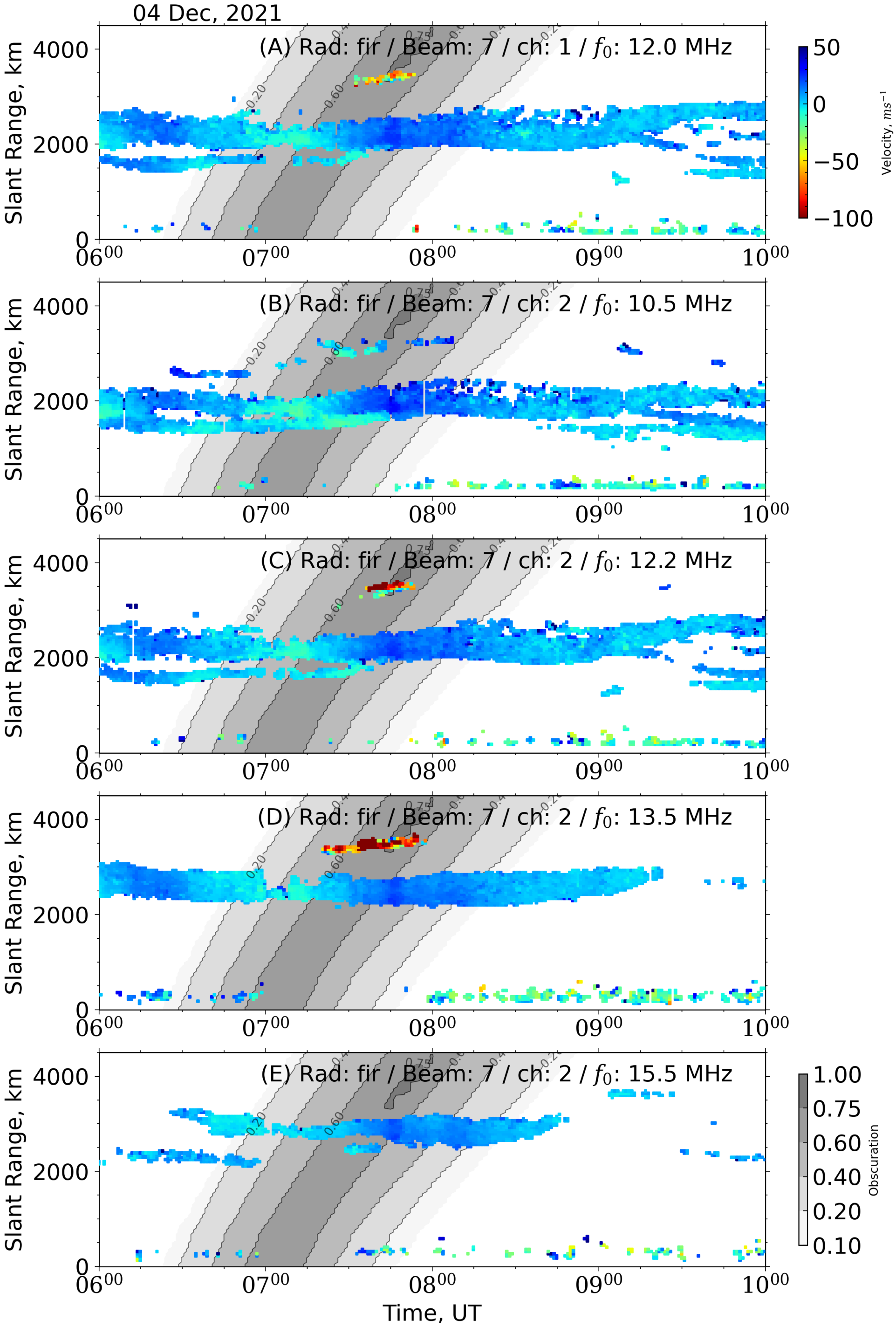

Figure 4. Range-time-intensity (RTI) plots of FIR beam 7 line-of-sight Doppler velocity on 04 December 2021 across five operating frequencies: (A) 12.0 MHz, channel 1; (B) 10.5 MHz, channel 2; (C) 12.2 MHz, channel 2; (D) 13.5 MHz, channel 2; (E) 15.5 MHz, channel 2. Eclipse obscuration contours (gray shading) are overlaid on each panel. The high-velocity ionospheric scatter population identified in Figure 1(C, D, E) appears as a coherent, strongly negative-Doppler patch near 3000–3800 km slant range between approximately 07:10 and 08:00 UT, but is absent at 10.5 MHz (B) and 15.5 MHz (E).

https://doi.org/10.5194/egusphere-2026-5257
Preprint. Discussion started: 14 September 2026

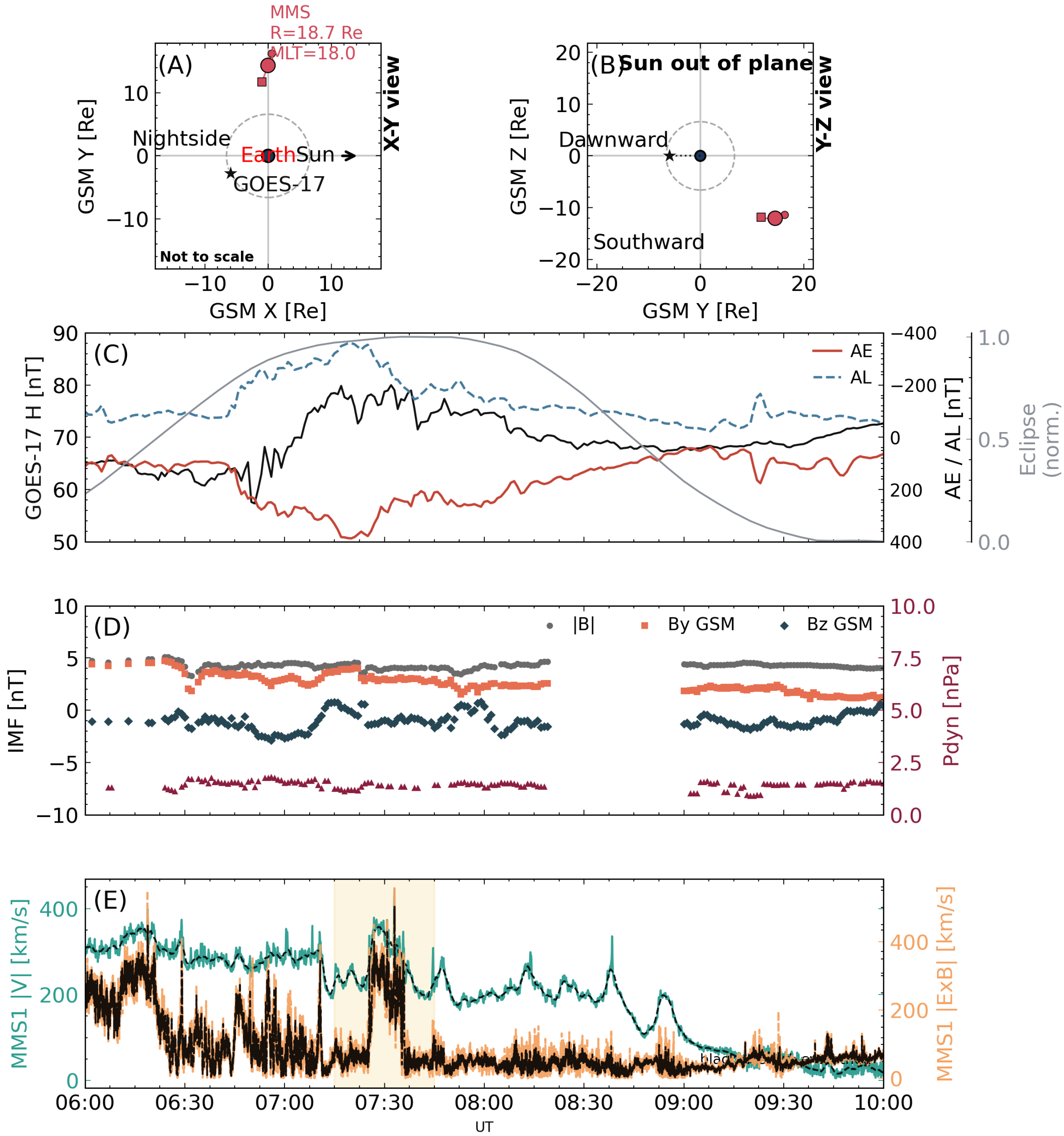

Figure 5. Consolidated overview of the 4 December 2021 eclipse interval from 06:00 to 10:00 UT. The top row shows MMS1 spacecraft location in GSM (A) X–Y and (B) Y–Z projections relative to Earth and GEO, with GOES-17 marked in the geosynchronous region; the Y–Z panel places GOES-17 on the $Z = 0$ equatorial line. (C) GOES-17 magnetic field H-component together with AE, AL and the eclipse obscuration proxy; (D) OMNI solar-wind and IMF conditions, including $|B|$, B_y, B_z, dynamic pressure. (E) MMS1 ion bulk speed and $E \times B$ speed, with a highlighted interval from 07:15 to 07:45 UT indicating the feature window of interest. Black dashed curves denote smoothed trends used to emphasize the temporal evolution of the MMS flows.

https://doi.org/10.5194/egusphere-2026-5257
Preprint. Discussion started: 14 September 2026

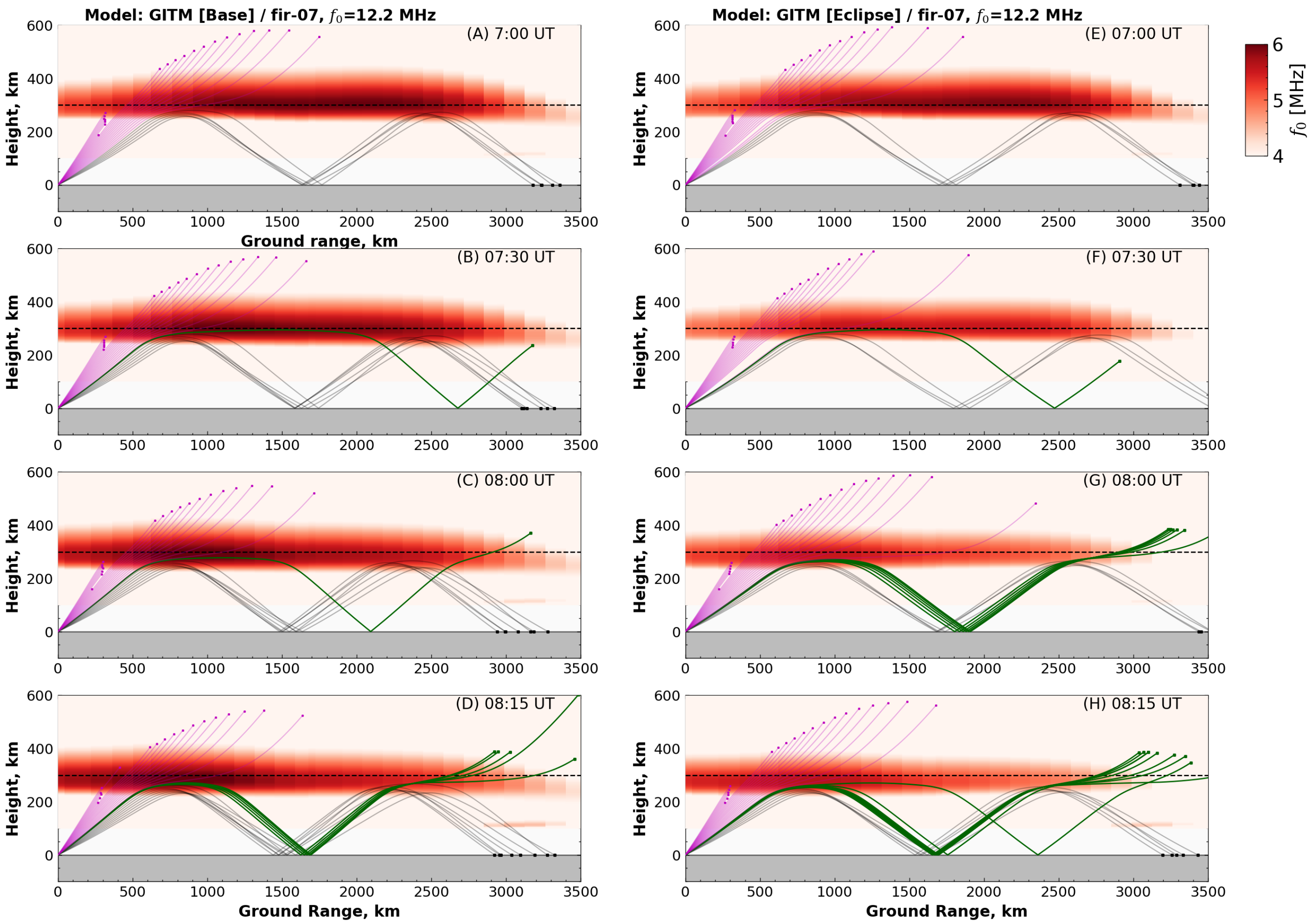

Figure 6. PHaRLAP ray-tracing simulation using GITM output through the base (left column) and eclipse-modified (right column) ionospheres. Panels (A–H) present ionospheric plasma density (color-coded by the scale in the top right), escaping rays (red), $\frac{1}{2}$-hop IS (magenta), ground scatter (black), and $1\frac{1}{2}$-hop IS (thick green).

B_z and J_y diagnostics in their eclipse-driven run, and instead attributed a shift of up to 16 R_E in the nightside last-closed-field-line position to a large-scale electrodynamic response — enhanced cross-polar-cap potential and anti-sunward flow driven by eclipse-reduced ionospheric conductance — rather than to intrinsic magnetotail instability. Coyle et al. (2023b) independently identified a geomagnetic substorm onset near 06:40 UT on 4 December 2021 from the AE index and a 40°-magnetic-meridian ground magnetometer array, roughly 60–65 minutes before local peak totality (07:44 UT); they attribute a separate, eclipse-coincident wave signature in TEC and ground magnetometer data to an eclipse effect rather than to this substorm, but their analysis does not establish whether the substorm onset itself was independent of the eclipse. GOES-17 H and the AE index in fact track the eclipse obscuration proxy closely in shape over this window (Panel C), and Coyle et al. (2023a) separately report a statistically significant population-level link between eclipse timing and substorm onset, so an eclipse contribution to

https://doi.org/10.5194/egusphere-2026-5257
Preprint. Discussion started: 14 September 2026

this substorm cannot be ruled out. Given this, whether the polar-cap electrodynamic reconfiguration described in Observations section (Figures 1–2) is driven by the eclipse, by the substorm, or by both together remains inconclusive. We note that the reconfiguration is observed poleward of the auroral oval boundary, within the polar cap rather than the auroral zone where substorm current-wedge signatures are typically strongest (Figure 1); FAC intensity, Φ[pyMIX], and MCM/Jang Bogo plasma flow nonetheless rise and fall in step with eclipse obscuration throughout the event, a temporal correspondence consistent with an eclipse contribution even though a substorm contribution cannot be excluded. This ambiguity is not unique to our dataset: an independent MHD-GCM simulation of the same event likewise could not attribute the accompanying substorm activity to the eclipse or rule it out, noting that eclipse-driven conductivity changes, independent magnetospheric processes, or some coupling of the two all remain plausible (Hong et al., 2026).

The enhanced plasma flow velocity observed by the MCM radar during the 2021 Antarctic eclipse is likely driven, at least in part, by eclipse-induced reductions in ionospheric conductance and associated reconfigurations of ionospheric current systems and field-aligned currents (FACs), which in turn may feed back into the magnetosphere. We examined 1-minute OMNI IMF and solar-wind parameters during the event (Figure 5) and found no coincident pressure pulse or IMF rotation that could externally drive the observed high-velocity plasma flows within the polar cap; solar wind dynamic pressure was, if anything, stable over this interval. This rules out direct solar-wind forcing as the origin of the flow enhancement, though it does not by itself distinguish between an eclipse-driven and a substorm-driven internal origin. At the population level, using a 20-year database of magnetometer observations and eclipse timings, Coyle et al. (2023a) demonstrated a statistically significant relationship between eclipse events and the occurrence of magnetospheric substorms, proposing that eclipse-induced reductions in ionospheric conductivity can act as a triggering mechanism for substorm onset and auroral-region ULF wave activity. As noted above (Figure 5), the ∼06:40 UT substorm onset in this event and the eclipse obscuration curve are not clearly separable in time, so Coyle et al. (2023a)'s statistical result raises the plausible possibility that eclipse and substorm forcing acted together in this event, rather than as independent alternatives; disentangling their relative contributions to the polar-cap electrodynamic reconfiguration is not possible from the present dataset alone.

A related study by Liu et al. (2021), focusing on solar flare impacts, demonstrated that flare-driven enhancements in ionospheric conductivity can lead to a *sudden drop* in the CPCP, as observed by SuperDARN radars and corroborated through numerical simulations. They argued that such reductions in CPCP must be accompanied by a corresponding decrease in the dayside magnetopause reconnection potential. Solar flares and solar eclipses represent opposite drivers, increasing versus decreasing conductance, respectively; nonetheless, these results provide a valuable conceptual framework for interpreting eclipse-driven effects observed in this study.

SuperDARN MCM radar observations reveal a significant increase in plasma flow velocity near the time of maximum eclipse, opposite in sign to the CPCP reductions reported during solar flares in Liu et al. (2021). As shown in Figure 3 (Observations section), the eclipse coincides with a significant enhancement in both FAC intensity and horizontal plasma flow velocities, despite a simultaneous reduction in ionospheric conductance. Under the classical voltage- and current-generator limits introduced above (Lysak, 1985), M–I coupling is modeled either as a fixed-CPCP or a fixed-FAC response to a conductance change. However, our observations during the eclipse show simultaneous increases in FACs and plasma flow velocities

https://doi.org/10.5194/egusphere-2026-5257
Preprint. Discussion started: 14 September 2026

without a proportional rise in CPCP, deviating from both idealized limits. This suggests that the system dynamically adjusts both electric fields and currents in response to eclipse-driven reductions in ionospheric conductance. These findings align with simulation-based evidence that the M–I system behaves as neither a pure current nor a pure voltage generator, but instead adjusts current and potential together in response to a conductance perturbation (Ridley et al., 2004; Liu et al., 2023). Our results highlight the complex electrodynamic feedback due to eclipse-driven conductance changes. Specifically, our observations are consistent with theoretical results showing that reduced Pedersen conductance enhances integrated FACs while simultaneously increasing CPCP, which is an indication of enhanced electric fields, thereby altering the M-I responses.

Finally, we turn to a second observational signature from Observations section: the new population of high-velocity ionospheric scatter (IS) that emerged at far ranges near the auroral oval, coincident with eclipse totality and modulated by the obscuration peak (Figure 1C–E). To examine one candidate driver of this feature, Figure 6 presents 2D PHaRLAP (Cervera and Harris, 2014) ray-tracing simulations along FIR beam 7 at 12.2 MHz, run through GITM-derived electron-density fields for the unperturbed base ionosphere (left column, panels A–D) and the eclipse-modified ionosphere (right column, panels E–H) at four times spanning the event (07:00, 07:30, 08:00, and 08:15 UT). In both columns, rays launched at high elevation angles escape through the topside ionosphere without returning to the ground, while rays launched at lower elevation angles refract back downward as conventional multi-hop ground scatter. Beginning around 07:30 UT (panels B, F), rays launched between roughly 20° and 40° elevation instead flatten out near the F-region density peak (dotted black line, ∼300 km) before continuing to a second hop, forming the $1\frac{1}{2}$-hop ray population (thick green traces). Within this subset, rays launched between 25° and 28° approach the density peak at near-grazing incidence, reaching the orthogonality condition needed for F-region backscatter near 350 km altitude. Comparing the base and eclipse columns at each time step, the $1\frac{1}{2}$-hop ray population is consistently denser and extends to farther ground ranges under the eclipse-modified density (panels G, H) than under the base ionosphere (panels C, D), an increase that grows through the sequence as eclipse obscuration deepens.

These $1\frac{1}{2}$-hop echoes, particularly the green rays in Figure 6, are consistent with Pedersen-mode rays (Ponomarenko et al., 2009; Ponomarenko and McWilliams, 2023), which duct parallel to the F-region peak during their first hop; their growing population under eclipse-modified density supports eclipse-driven changes in the ionospheric refractive index as a plausible mechanism opening this propagation path to the auroral oval. A second potential mechanism involves soft monoenergetic particle precipitation in the auroral zone (Chen et al., 2021), which SuperDARN radars are known to detect as precipitation signatures at these latitudes (Ponomarenko and Waters, 2006). Coyle et al. (2023b) reported step-like enhancements in slant TEC in this region that tracked eclipse obscuration, together with a sudden increase in ULF wave power in the 20–40 mHz (PC3) band across multiple Antarctic ground stations, likewise modulated by eclipse obscuration and persisting primarily between 07:30–08:30 UT; they attribute this wave and TEC activity to an eclipse effect rather than to the ∼06:40 UT substorm identified in the same interval. We follow that attribution in tying this candidate precipitation mechanism to the eclipse-timed wave/TEC activity itself. While both mechanisms may be acting in tandem, resolving their relative contributions will require a fully coupled M-I simulation, integrated with HF ray tracing and auroral precipitation models, which is beyond the scope of this endeavor. In any case, the GITM + PHaRLAP simulation (which does not include M–I coupling) replicates the emergence of this ionospheric scatter as a consequence of eclipse-reduced electron density alone.

https://doi.org/10.5194/egusphere-2026-5257
Preprint. Discussion started: 14 September 2026

The frequency-selective appearance of this scatter (Figure 4) offers an additional, independent constraint on the refractive-index mechanism proposed above. The $1\frac{1}{2}$-hop, Pedersen-mode ray path identified by the PHaRLAP simulations requires the wave frequency to be high enough to penetrate the reduced-density F-region without full reflection, yet low enough to still achieve near-orthogonality with the ray path close to the F-region peak; eclipse-driven electron-density depletion narrows or shifts this window rather than removing it. That the high-velocity scatter is confined to 12.0–13.5 MHz and absent at 10.5 MHz and 15.5 MHz is qualitatively consistent with such a bounded propagation window: at 10.5 MHz the reduced density may still be sufficient to reflect the ray before it reaches the required grazing geometry, while at 15.5 MHz the ray may instead escape rather than duct along the F-region peak. A quantitative test of this interpretation, extending the PHaRLAP ray-tracing simulations of Figure 6 to the additional FIR operating frequencies shown in Figure 4, is planned as follow-on work.

5 Conclusions

This study presents new observational evidence that suggests the possibility of eclipse-driven electrodynamic reconfiguration and propagation effects in the south polar ionosphere during the 2021 Antarctic solar eclipse, based on multi-instrument SuperDARN, VIPIR, and AMPERE observations. Enhanced anti-sunward plasma flow velocities were observed within the polar cap by the MCM radar and the Jang Bogo station, together with an increase in AMPERE-derived field-aligned currents (FACs) and fitted polar-cap potential. Observations and modeling efforts suggest eclipse-induced reductions in ionospheric conductance may drive a subsequent reconfiguration of the coupled M–I system, which responds not as a pure current or voltage source, but through complex spatial and temporal restructuring of conductance and electric fields.

Separately, we report systematic swings in line-of-sight Doppler velocities and the emergence of a new population of high-velocity ionospheric scatter (IS) near the auroral oval, temporally aligned with the eclipse maximum. These IS features exhibit spatial motion that tracks the eclipse path, suggesting activation of a distinct propagation mode enabled by eclipse-modified ionospheric conditions. PHaRLAP ray tracing using eclipse obscuration-driven GITM-simulated electron densities reveals that Pedersen-mode rays with $\sim25°$–$28°$ elevation angles reach backscatter heights near 350 km through $1\frac{1}{2}$-hop propagation, offering one explanation for the observed high-velocity IS. Alternatively, soft particle precipitation coincident with eclipse-timed wave and TEC activity may also contribute. As the Moon's shadow swept past and sunlight returned, the coupled M–I system relaxed back toward its pre-eclipse state, a brief, natural reminder of how tightly ionospheric electrodynamics and radio propagation are bound to the Sun's illumination.

6 List of abbreviations

– AMPERE: Active Magnetosphere and Planetary Electrodynamics Response Experiment

– CPCP: Cross-Polar-Cap Potential

– FAC(s): Field-Aligned Current(s)

https://doi.org/10.5194/egusphere-2026-5257
Preprint. Discussion started: 14 September 2026

- FIR: Falkland Islands Radar (SuperDARN)
- GITM: Global Ionosphere Thermosphere Model
- GNSS: Global Navigation Satellite System
- GS: Ground Scatter
- GSM: Geocentric Solar Magnetospheric (coordinate system)
- HF: High Frequency
- IMF: Interplanetary Magnetic Field
- IS: Ionospheric Scatter
- IT: Ionosphere–Thermosphere
- LoS: Line-of-Sight
- M–I: Magnetosphere–Ionosphere
- MCM: McMurdo (SuperDARN radar)
- MMS: Magnetospheric Multiscale (mission)
- PHaRLAP: Provision of a High-frequency Raytracing Laboratory for Propagation studies
- pyMIX: Python Magnetosphere–Ionosphere eXchange (potential solver)
- SuperDARN: Super Dual Auroral Radar Network
- TEC: Total Electron Content
- ULF: Ultra-Low Frequency
- UT: Universal Time
- VIPIR: Vertical Incidence Pulsed Ionospheric Radar

Code and data availability. All the data, simulation results, and code are uploaded into the Zenodo repository and are available for public use (Chakraborty, 2026). Most of the analysis and visualization were completed with the help of free, open-source software tools such as matplotlib (Hunter, 2007), IPython (Perez and Granger, 2007), pandas (McKinney, 2010), pyDARN (Shi et al., 2022), and others (e.g., Millman and Aivazis, 2011). The eclipse obscuration mask has been computed with PyEclipse software freely available at Zenodo (Mrak et al., 2022). We thank all participants in the worldwide SuperDARN collaboration for the distribution of SuperDARN data via http://vt.superdarn.org/.

IMF, solar wind parameters, and geomagnetic conditions observations were obtained from the OMNI website: https://omniweb.gsfc.nasa.gov (Papitashvili and King, 2020).

Author contributions. SC conceived the study and funding acquisition, performed the primary data analysis, and wrote the original draft. SM developed eclipse obscuration modeling (PyEclipse) and contributed the GITM simulations. AC developed the pyMIX potential-solver methodology. EGT contributed SuperDARN data processing and software support. GC provided and supported the Falkland Islands (FIR) radar data. WB provided and supported the McMurdo (MCM) radar data. AB contributed to supervision and funding acquisition. All authors reviewed and edited the manuscript.

Competing interests. The authors declare that they have no competing financial or personal interests that could have appeared to influence the work reported in this paper.

Financial support. SC thanks to the National Science Foundation (NSF) and NASA for support under grants AGS-2512183 and 80NSSC19K0773 respectively. SC is also supported by Center for Space and Atmospheric Research at ERAU. SM thanks the support from NSF AGS- 2412295, NASA grants 80NSSC24K1268, 80NSSC19K0773, and AFOSR FA9550-24-1-0013. AC acknowledges support from NSF grant # 2426201. EGT acknowledges support from the National Science Foundation under Grants AGS-1934997 and AGS-2426199, and the Office of Naval Research under Grant N000142312109.

Acknowledgements. The Falkland Islands radar is maintained and operated by the British Antarctic Survey with support from the UK Natural Environment Research Council (NERC) under the PRESCIENT project (NE/Y006178/1). We acknowledge the use of SuperDARN data. SuperDARN is a network of radars funded by the national scientific funding agencies of Australia, Canada, China, France, Italy, Japan, Norway, South Africa, the United Kingdom, and the United States of America. The authors used an AI-based language assistant for grammar and sentence-construction support during manuscript preparation; all scientific content, analysis, and interpretation are the authors' own.

https://doi.org/10.5194/egusphere-2026-5257
Preprint. Discussion started: 14 September 2026

References

Anderson, B. J., Takahashi, K., and Toth, B. A.: Sensing global Birkeland currents with Iridium engineering magnetometer data, Geophysical Research Letters, 27, 4045–4048, https://doi.org/10.1029/2000GL000094, 2000.

Cantrall, C. E., Mrak, S., Paxton, L. J., Zhang, Y., Nikoukar, R., Schaefer, R. K., and Yee, J. H.: Source of the Observed Enhancements in Thermospheric ΣO/N2 During Two Solar Eclipses in 2023, Journal of Geophysical Research: Space Physics, 129, https://doi.org/10.1029/2024JA032542, 2024.

Cervera, M. A. and Harris, T. J.: Modeling ionospheric disturbance features in quasi-vertically incident ionograms using 3-D magnetoionic ray tracing and atmospheric gravity waves, J. Geophys. Res. Space Physics, 119, 431–440, https://doi.org/10.1002/2013JA019247, 2014.

Chakraborty, S.: shibaji7/eclipse_analysis, Zenodo, https://doi.org/10.5281/zenodo.18749988, 2026.

Chakraborty, S., Qian, L., Mrak, S., Mabie, J., Goncharenko, L., Mclnerney, J. M., and Bullett, T.: Formation of the Ionospheric G-Condition Following the 2017 Great American Eclipse, Earth and Space Science, 12, https://doi.org/10.1029/2024EA004007, 2025.

Chartier, A. T., Huba, J. D., Sitaram, D. P., Merkin, V. G., Anderson, B. J., and Vines, S. K.: High-Latitude Electrodynamics Specified in SAMI3 Using AMPERE Field-Aligned Currents, Space Weather, 20, https://doi.org/10.1029/2021SW002890, 2022.

Chen, X., Dang, T., Zhang, B., Lotko, W., Pham, K., Wang, W., et al.: Global effects of a polar solar eclipse on the coupled magnetosphere-ionosphere system, Geophysical Research Letters, 48, https://doi.org/10.1029/2021gl096471, article e2021GL096471, 2021.

Chisham, G., Lester, M., Milan, S. E., Freeman, M. P., Bristow, W. A., Grocott, A., McWilliams, K. A., Thornhill, J. D., Dyson, P. L., Greenwald, R. A., Sofko, G. J., Villain, J. P., and Walker, A. D. M.: A decade of the Super Dual Auroral Radar Network (SuperDARN): Scientific achievements, new techniques and future directions, Surveys in Geophysics, 28, 33–109, https://doi.org/10.1007/s10712-007-9017-8, 2007.

Choudhary, R. K., Tiwari, D., Maurya, A. K., et al.: The impact of the January 15, 2010 annular solar eclipse on the equatorial and low-latitude ionosphere over the Indian region, Journal of Geophysical Research: Space Physics, 116, A11 304, https://doi.org/10.1029/2011JA016821, 2011.

Cnossen, I., Ridley, A., Goncharenko, L., and Harding, B.: The response of the ionosphere-thermosphere system to the 21 August 2017 solar eclipse, Journal of Geophysical Research: Space Physics, 124, 7341–7355, https://doi.org/10.1029/2018ja026402, 2019.

Coroniti, F. V. and Kennel, C. F.: Can the ionosphere regulate magnetospheric convection?, Journal of Geophysical Research, 78, 2837–2851, https://doi.org/10.1029/JA078i016p02837, 1973.

Coyle, S. E., Baker, J. B. H., Chakraborty, S., Hartinger, M. D., Freeman, M. P., Clauer, C. R., et al.: Substorms and solar eclipses: A mutual information based study, Geophysical Research Letters, 50, e2023GL106432, https://doi.org/10.1029/2023GL106432, 2023a.

Coyle, S. E., Hartinger, M. D., Clauer, C. R., Baker, J. B. H., Cnossen, I., Freeman, M. P., and Weygand, J. M.: The 2021 Antarctic total eclipse: Ground magnetometer and GNSS wave observations from the 40 degree magnetic meridian, Journal of Geophysical Research: Space Physics, 128, e2022JA031142, https://doi.org/10.1029/2022JA031142, 2023b.

Ergun, R. E., Tucker, S., Westfall, J., Goodrich, K. A., Malaspina, D. M., Summers, D., Wallace, J., Karlsson, M., Mack, J., Brennan, N., et al.: The Axial Double Probe and Fields Signal Processing for the MMS Mission, Space Science Reviews, 199, 167–188, https://doi.org/10.1007/s11214-014-0115-x, 2016.

Greenwald, R. A., Baker, K. B., Hutchins, R. A., and Hanuise, C.: An HF phased-array radar for studying small-scale structure in the high-latitude ionosphere, Radio Science, 20, 63–79, https://doi.org/10.1029/RS020i001p00063, 1985.

Hong, Y., Deng, Y., Welling, D. T., Ridley, A. J., Lu, G., Maute, A., Zhu, Q., Mrak, S., Waters, C., Sheng, C., Li, M., and Lopez, R.: Impacts of Ionospheric Conductance During the December 2021 Solar Eclipse on the Coupled Magnetosphere-Ionosphere-Thermosphere System, Journal of Geophysical Research: Space Physics, 131, e2026JA035 392, https://doi.org/https://doi.org/10.1029/2026JA035392, e2026JA035392 2026JA035392, 2026.

Huang, C.-S., Foster, J. C., Zhang, S.-R., Erickson, P. J., and Vierinen, J.: Ionospheric responses at low latitudes to the annular solar eclipse on 21 June 2020, Journal of Geophysical Research: Space Physics, 125, https://doi.org/10.1029/2020JA028337, article e2020JA028337, 2020.

Hunter, J. D.: Matplotlib: A 2d graphics environment, Computing in Science & Engineering, 9, 90–95, https://doi.org/10.1109/MCSE.2007.55, 2007.

Hvoždara, M. and Prigancová, A.: Geomagnetic effects due to an eclipse-induced low-conductivity ionospheric spot, Journal of Geophysical Research, 107, 1467, https://doi.org/10.1029/2002JA009260, 2002.

Kim, K. H., Kim, D. H., Back, J., Kwon, H. J., Jee, G., Ham, Y. B., Lee, C., and Kim, J. H.: Dynasonde Observations of Ionospheric Polar Holes Under Quiet Geomagnetic Conditions at Jang Bogo Station, Antarctica, Journal of Geophysical Research: Space Physics, 128, https://doi.org/10.1029/2023JA031563, 2023.

Lindqvist, P.-A., Olsson, G., Torbert, R. B., King, B., Granoff, M., Rau, D., Needell, G., Turco, S., Dors, I., Beckman, P., et al.: The Spin-Plane Double Probe Electric Field Instrument for MMS, Space Science Reviews, 199, 137–165, https://doi.org/10.1007/s11214-014-0116-9, 2016.

Liu, J., Wang, W., Qian, L., et al.: Solar flare effects in the Earth's magnetosphere, Nat. Phys., 17, 807–812, https://doi.org/10.1038/s41567-021-01203-5, 2021.

Liu, J., Wang, W., Qian, L., Pham, K., Liu, L., Li, Q., Li, S., and Liu, X.: Impacts of Ionospheric Conductance on Magnetosphere-Ionosphere Coupling, Journal of Geophysical Research: Space Physics, 128, e2022JA030 864, https://doi.org/10.1029/2022JA030864, 2023.

Lysak, R. L.: Auroral electrodynamics with current and voltage generators, Journal of Geophysical Research: Space Physics, 90, 4178–4190, https://doi.org/10.1029/JA090iA05p04178, 1985.

McKinney, W.: Data structures for statistical computing in python, in: Proceedings of the 9th Python in science conference, pp. 56–61, https://doi.org/10.25080/Majora-92bf1922-012686, 2010.

Millman, K. J. and Aivazis, M.: Python for scientists and engineers, Computing in Science & Engineering, 13, 2, https://doi.org/10.1109/MCSE.2011.36, 2011.

Moses, M. L., Kordella, L. J., Earle, G. D., Drob, D., Huba, J. D., Ruohoniemi, J. M., et al.: Observations and modeling studies of solar eclipse effects on oblique high frequency radio propagation, Space Weather, 19, e2020SW002560, https://doi.org/10.1029/2020SW002560, 2021.

Mrak, S., Semeter, J., Drob, D., and Huba, J. D.: Direct EUV/X-ray modulation of the ionosphere during the august 2017 total solar eclipse, Geophysical Research Letters, 45, 3820–3828, https://doi.org/10.1029/2017GL076771, 2018.

Mrak, S., Zhu, Q., Deng, Y., Dammasch, I. E., Dominique, M., Hairston, M. R., Nishimura, Y., and Semeter, J.: Modeling Solar Eclipses at Extreme Ultra Violet Wavelengths and the Effects of Nonuniform Eclipse Shadow on the Ionosphere-Thermosphere System, Journal of Geophysical Research: Space Physics, 127, https://doi.org/10.1029/2022JA031058, article e2022JA031058, 2022.

Newell, P. T., Sotirelis, T., Meng, C.-I., and Lyons, K. M.: Auroral precipitation characteristics from DMSP particle data: Model and overview, Journal of Geophysical Research: Space Physics, 101, 25 957–25 971, https://doi.org/10.1029/96JA02620, 1996.

Newell, P. T., Sotirelis, T., and Wing, S.: Diffuse, monoenergetic, and broadband aurora: The global precipitation budget, Journal of Geophysical Research: Space Physics, 114, A09 207, https://doi.org/10.1029/2009JA014326, 2009.

https://doi.org/10.5194/egusphere-2026-5257
Preprint. Discussion started: 14 September 2026

Nishitani, N., Ruohoniemi, J. M., Lester, M., Baker, J. B. H., Koustov, A. V., Shepherd, S. G., Bristow, W. A., Hori, T., Thomas, E. G., Makarevich, R. A., Ponomarenko, P. V., St-Maurice, J. P., Ogawa, T., Shiokawa, K., Otsuka, Y., Milan, S. E., Wild, J. A., Ribeiro, A. J., and Kikuchi, T.: Review of the accomplishments of mid-latitude Super Dual Auroral Radar Network (SuperDARN) HF radars, Progress in Earth and Planetary Science, 6, https://doi.org/10.1186/s40645-019-0270-5, article 27, 2019.

Papitashvili, N. E. and King, J. H.: Omni 1-min data [data set], NASA SpacePhysics Data Facility. (Accessed on (June, 2024, https://doi.org/10.48322/45bb-8792707, 2020.

Perez, F. and Granger, B. E.: Ipython: A system for interactive scientific computing, Computing in Science & Engineering, 9, 3, https://doi.org/10.1109/MCSE.2007.53, 2007.

Pollock, C., Moore, T., Jacques, A., Burch, J., Gliese, U., Saito, Y., Omoto, T., Avanov, L., Barrie, A., Coffey, V., et al.: Fast Plasma Investigation for Magnetospheric Multiscale, Space Science Reviews, 199, 331–406, https://doi.org/10.1007/s11214-016-0245-4, 2016.

Ponomarenko, P. and McWilliams, K. A.: Climatology of HF propagation characteristics at very high latitudes from SuperDARN observations, Radio Science, 58, e2023RS007657, https://doi.org/10.1029/2023RS007657, 2023.

Ponomarenko, P. V. and Waters, C. L.: Spectral width of SuperDARN echoes: measurement, use and physical interpretation, Ann. Geophys., 24, 115–128, https://doi.org/10.5194/angeo-24-115-2006, 2006.

Ponomarenko, P. V., Waters, C. L., and Menk, F. W.: Factors determining spectral width of HF echoes from high latitudes, Ann. Geophys., 25, 675–687, https://doi.org/10.5194/angeo-25-675-2007, 2007.

Ponomarenko, P. V., St-Maurice, J.-P., Waters, C. L., Gillies, R. G., and Koustov, A. V.: Refractive index effects on the scatter volume location and Doppler velocity estimates of ionospheric HF backscatter echoes, Ann. Geophys., 27, 4207–4219, https://doi.org/10.5194/angeo-27-4207-2009, 2009.

Ridley, A. J., Gombosi, T. I., and DeZeeuw, D. L.: Ionospheric control of the magnetosphere: conductance, Annales Geophysicae, 22, 567–584, https://doi.org/10.5194/angeo-22-567-2004, 2004.

Rishbeth, H.: Solar eclipses and ionospheric theory, Space Science Reviews, 8, 543–554, https://doi.org/10.1007/BF00175006, 1968.

Shi, X., Schmidt, M., Martin, C. J., Billett, D. D., Bland, E., Tholley, F. H., Frissell, N. A., Khanal, K., Coyle, S., Chakraborty, S., Detwiller, M., Kunduri, B., and McWilliams, K.: pyDARN: A Python software for visualizing SuperDARN radar data, Front. Astron. Space Sci., 9, https://doi.org/10.3389/fspas.2022.1022690, article 1022690, 2022.

Singer, H., Matheson, L., Grubb, R., Newman, A., and Bouwer, D.: Monitoring space weather with the GOES magnetometers, Proceedings of SPIE, GOES-8 and Beyond, 2812, 299–308, https://doi.org/10.1117/12.254077, 1996.

Siscoe, G. L., Erickson, G. M., Sonnerup, B. U. Ö., Maynard, N. C., Schoendorf, J. A., Siebert, K. D., Weimer, D. R., White, W. W., and Wilson, G. R.: Hill model of transpolar potential saturation: Comparisons with MHD simulations, Journal of Geophysical Research, 107, https://doi.org/10.1029/2001JA000109, 2002.

Sun, Y., Wang, H., and Zhang, S.: Nighttime ionosphere perturbed by the annular solar eclipse on June 21, 2020, Journal of Geophysical Research: Space Physics, 126, e2021JA029305, https://doi.org/10.1029/2021JA029305, 2021.

Thomas, E. G., Shepherd, S. G., Kunduri, B. S. R., and Themens, D. R.: Multi-frequency SuperDARN HF radar observations of the ionospheric response to the October 2023 annular solar eclipse, Geophysical Research Letters, 51, e2024GL112450, https://doi.org/10.1029/2024GL112450, 2024.

Weimer, D. R.: Improved ionospheric electrodynamic models and application to calculating Joule heating rates, Journal of Geophysical Research: Space Physics, 110, 1–21, https://doi.org/10.1029/2004JA010884, 2005.

https://doi.org/10.5194/egusphere-2026-5257
Preprint. Discussion started: 14 September 2026

Wolf, R. A.: Effects of ionospheric conductivity on convective flow of plasma in the magnetosphere, Journal of Geophysical Research, 75, 4677–4698, https://doi.org/10.1029/JA075i025p04677, 1970.

Zhu, Q., Deng, Y., Maute, A., Kilcommons, L. M., Knipp, D. J., and Hairston, M.: ASHLEY: A New Empirical Model for the High-Latitude Electron Precipitation and Electric Field, Space Weather, 19, 1–25, https://doi.org/10.1029/2020SW002671, 2021.